

About the Impact of Defect Phases on the Thermoelectric Properties of $\text{Cr}_3\text{S}_{4-x}\text{Se}_x$

Hendrik Groß,* Dennis Groeneveld, Michael Poschmann, Ulrich Schürmann, Jan D. König, Wolfgang Bensch, Jürgen Wöllenstein, and Lorenz Kienle*

Phase relations in Cr_3S_4 and the substituted system $\text{Cr}_3\text{S}_{4-x}\text{Se}_x$ are studied to determine the influence of chemical substitutions on the thermoelectric properties. In addition to the expected equilibrium phase crystallizing in the monoclinic space group $I2/m$, some samples exhibit a defect phase with Cr_2S_3 -like structure. The defect phase can be observed in a few samples prior to sintering, with the majority being phase-pure Cr_3S_4 . The defect phase can, however, be introduced in phase-pure samples through in situ heating. It can be proven that the defect phase has an influence on the thermoelectric properties, by lowering the electrical and thermal conductivity, while increasing the Seebeck coefficient. Substitution in the anion lattice of Cr_3S_4 with Se lowers the thermal conductivity. The improvement is mainly achieved through a reduction of the electronic contribution to the thermal conductivity, leading to total values as low as $1.6 \text{ W m}^{-1} \text{ K}^{-1}$ for the substituted system in comparison to the pristine material $2.3 \text{ W m}^{-1} \text{ K}^{-1}$.

1. Introduction

Understanding the complex interrelation between composition, crystal structure and the resulting electrical and thermal properties is key to developing an efficient thermoelectric material. Chromium sulfides and selenides exhibit thermoelectric properties as well as a large variety in structure, which presents an ideal opportunity to investigate this interrelation and its influence on the thermoelectric behavior.^[1–3] Additionally, their constituents Cr, S, and Se are available in high abundance, while their environmental footprint regarding toxicity remains reasonably low. In general, chromium chalcogenides appear as pseudo-layered compounds, comprising alternating layers with either full or partial occupations of the metal-

cation positions.^[4] The respective occupation of the partially occupied layers as well as their stacking order lead to different electrical properties, which facilitate different applications: Cr_2S_3 , for example, exhibits poor semiconducting behavior, while the investigated Cr_3S_4 shows an electrical conductivity in the range of metals, due to a partially filled conduction band.^[5,6] Either way, the crystal structure is reported to remain in its pristine state after doping and/or atom substitution, which allows to manipulate and fine-tune the thermoelectric properties and therefore to enhance their performance and efficiency. In turn, the structural variety often presents a challenge for synthesis and investigation, as many compounds in the Cr–S–Se system often exhibit a very narrow stability range for the respective chalcogen content before forming a different phase. The phase region for Cr_3S_4 remains largely unknown, especially regarding the behavior in case of stoichiometric deviations.^[7,8] In literature, the phase regions, in which a composition of Cr_3S_4 can be expected, are reported with differing tolerances: Waldner et al.^[9] describe the system as a singular line phase, while other reports suggest it to exist within a range of 56%–58% of sulfur content.^[4,10–12] Investigations on Cr_3Se_4 with varying Cr content indicate a broader phase region compared to Cr_3S_4 .^[13–16]


Due to this, stoichiometric deviations and inhomogeneities may lead to a phase transformation or the occurrence of an additional phase.^[13] In this study, a phase was observed to occur in as-synthesized powders prior to sintering, possibly originating from deviations in the S content, which we call defect phase. This defect phase is structurally related to Cr_2S_3 , which crystallizes in

H. Groß, U. Schürmann, L. Kienle
 Department of Materials Science
 Kiel University
 Kaiserstr. 2, 24143 Kiel, Germany
 E-mail: hegr@tf.uni-kiel.de; lk@tf.uni-kiel.de

D. Groeneveld, J. D. König, J. Wöllenstein
 Laboratory for Gas Sensors
 IMTEK – Department of Microsystems Engineering
 University of Freiburg
 Georges-Koehler-Allee 102, 79110 Freiburg, Germany

M. Poschmann, W. Bensch
 Institute of Inorganic Chemistry
 Kiel University
 Max-Eyth-Str. 2, 24118 Kiel, Germany

J. D. König
 Department of Thermal Energy Converters
 Fraunhofer Institute for Physical Measurement Techniques IPM
 Georges-Koehler-Allee 301, 79110 Freiburg, Germany

 The ORCID identification number(s) for the author(s) of this article can be found under <https://doi.org/10.1002/adem.202201505>.

© 2023 The Authors. Advanced Engineering Materials published by Wiley-VCH GmbH. This is an open access article under the terms of the Creative Commons Attribution-NonCommercial License, which permits use, distribution and reproduction in any medium, provided the original work is properly cited and is not used for commercial purposes.

DOI: 10.1002/adem.202201505

space group $R\bar{3}$. Assuming that the $R\bar{3}$ structure is formed with Cr_3S_4 stoichiometry, this leads to a Cr excess in the partially occupied layers compared to the occupancy found in stoichiometric Cr_3S_4 . The additional Cr atoms can relax by occupying empty positions in the partially filled layer, thus leading to disorder of all Cr interlayer positions. To illustrate the general structural relationship as well as the changes occurring in the defect phase, both structures are shown as a schematic representation in **Figure 1**.

In both cases, the structure is comprised of CrS_6 octahedra, which form a sequence of fully occupied layers (blue) alternating with partially occupied interlayers. For Cr_3S_4 in its equilibrium phase ($I2/m$), these defective layers are occupied by Cr^{2+} cations and ordered in a twofold stacking sequence. If the interlayer Cr positions are disordered and the Cr_2S_3 phase is formed, the oxidation state of the interlayer cations changes to Cr^{3+} , while the stacking sequence in the expected space group $R\bar{3}$ is now threefold.^[4,6,17–19]

The layered topology is generally favorable for a thermoelectric material, as it creates a confinement state at the boundary between fully occupied and defect layers. This facilitates a low lattice thermal conductivity orthogonal to the layers, that is, in c -direction, while the cations within the defect layers retain a high level of mobility.^[20–22] Low thermal conductivities have been stated for pristine Cr_3S_4 ,^[22,23] with literature reporting a Seebeck coefficient between -24 and $-36 \mu\text{V K}^{-1}$ ^[12,18] and an electrical conductivity with substantial variations. While Bouchard and Wold^[18] reported a semiconductor-like electrical conductivity of 167 S cm^{-1} , van Bruggen and Tazuke determined significantly higher values of 526 S cm^{-1} or even 1367 S cm^{-1} .^[7,12]

To achieve the highest possible thermoelectric performance, the synthesis and densification methods have to be performed carefully. High electrical conductivities can only be achieved if the relative density of the material is high, that is, ideally above 95%,^[3,24] while significant deviations in stoichiometry may lead

to unwanted phases and therefore a decline in electrical conductivity. In previous studies, chromium sulfides have shown volatilization losses of S during prolonged sintering, which could successfully be addressed with a new sintering method developed by our group.^[25,26] Some as-synthesized samples further exhibited traces of a Cr_2S_3 -like defect phase—previous studies revealed that sintering can be applied as a means to remove an existing defect phase, which was also taken into consideration here.^[26] In contrast, additional phases or atom impurities may prove beneficial for the thermal conductivity, which is lowered by introducing additional scattering centers for phonons. This has been applied to the structurally similar system NiCr_2S_4 in previous studies^[27] with substitutions in the cation sublattice. Pisharody et al. proved that substitutions in the anion sublattice (i.e., S replaced by Se) could also positively impact the thermoelectric performance by reducing the thermal conductivity.^[28] Cr_3S_4 and Cr_3Se_4 are isostructural,^[22,23,29] which allows the formation of solid solutions. These solid solutions can create additional boundaries in the material through planar defects, while a random distribution of Se in the S host matrix may lead to scattering centers due to the differences in atomic radii between S and Se.

In this study, we investigate the complex phase relations in the Cr_3S_4 system and the influence of synthesis and sintering methods as well as the resulting material's microstructure. The specially developed high-pressure sintering method for chromium sulfides, combining field-assisted sintering (FAST) and titanium–zirconium–molybdenum (TZM) tools, is applied to Cr_3S_4 . The influence of the Cr_2S_3 -like defect phase is investigated, as well as possible means of homogenization via tempering and sintering. Further, partial substitution in the anion lattice with Se is applied, resulting in the system $\text{Cr}_3\text{S}_{4-x}\text{Se}_x$. The influences on structure and thermoelectric properties are investigated, as well as the impact on the occurrence and stability of the defect phase.

2. Results and Discussion

2.1. X-Ray Diffraction

After high-temperature synthesis, the powdered materials of Cr_3S_4 and $\text{Cr}_3\text{S}_{4-x}\text{Se}_x$ were checked for chemical composition and structural properties with energy-dispersive X-ray spectroscopy (EDX) and X-ray diffraction (XRD). In some cases of Cr_3S_4 samples, minor phase impurities of $<2 \text{ wt}\%$ Cr_2O_3 and $<4 \text{ wt}\%$ of an $R\bar{3}$ defect phase (structure shown in **Figure 1**) were detected. Despite the $R\bar{3}$ crystal structure, which represents the equilibrium phase of Cr_2S_3 , the stoichiometry of the defect phase shows no deviations from the target composition of Cr_3S_4 . The structural description of the defect phase has therefore been developed based on the structure of Cr_2S_3 in $R\bar{3}$,^[6] with calculated reflection positions fitting very well to the observed ones for the structure. By allowing a significantly lowered occupancy of Cr1 in the partly occupied Cr layer and a high micro-strain, the intensities and reflection width of the observed additional reflections, underneath the reflections of the Cr_3S_4 $I2/m$ phase, can be satisfactorily modeled (structural parameters are given in Table S1, Supporting Information, and diffraction patterns in **Figure S14**, Supporting Information).

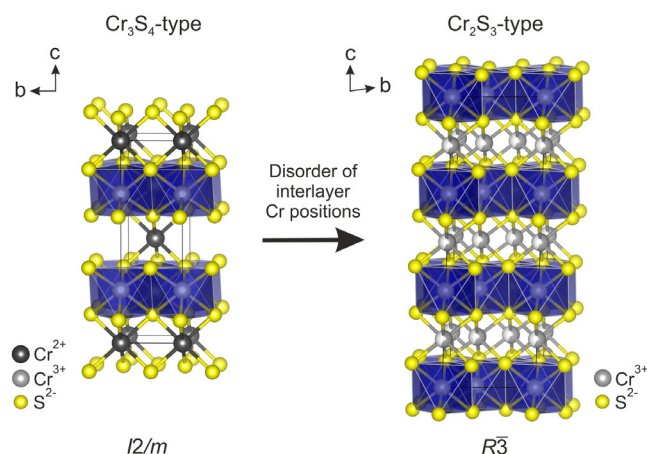


Figure 1. Schematic representation of the Cr_3S_4 structure (left) in comparison to the Cr_2S_3 -like structure of the defect phase (right), viewed in a -direction. Both structures are comprised of fully occupied layers of CrS_6 octahedra (blue), which alternate with partially occupied layers of Cr cations. In case of the Cr_2S_3 structure, Cr_3S_4 stoichiometry is achieved by occupying all interlayer positions to a degree of 56.25%, as indicated by the partially colored atoms. Image created with,^[38] based on crystallographic reference data obtained from Ref. [18].

Se substitution of S in Cr_3S_4 was successful and no formation of a defect phase was observed, that is, the samples were obtained phase pure. To investigate the thermal behavior of the synthesized Cr_3S_4 powder, it was investigated with XRD under He atmosphere at ambient pressure when heated up to 773 K and cooled back to room temperature (RT) (see Figure S1, Supporting Information). Rietveld refinement of the patterns shows that, when heated up, the unit cell parameters a , b , and c are enlarged and the monoclinic angle β decreases while overall the unit cell volume is expanded. At temperatures above 423 K, the occupancy of Cr1 in the partially filled layer apparently decreases, which can be interpreted as increasing disorder caused by thermally activated atom movement. Correlation of increasing atomic movement with increasing temperature is as well visible as increasing Debye–Waller factors of Cr and S atoms. All these changes in structural parameters also affect the atomic positions, which are altered with increasing temperature. The apparent micro-strain seems to be not affected in this temperature range. After cooling down to RT, all lattice parameters are slightly smaller than their initial values, and especially the apparent occupancy of the Cr1 atomic position remains on a low value (see Figure S2, Supporting Information). This indicates that the expansion of the unit cell and the increase in disorder of the Cr1 atom, as observed during heating, are irreversible, likely due to a decomposition process. Additionally, at temperatures above 673 K, reflections of a $\text{Cr}_3\text{S}_{4-x}$ phase in the $P\bar{3}1c$ structure appear. As Cr_5S_6 crystallizes in the same space group, the occurrence of the $\text{Cr}_3\text{S}_{4-x}$ phase can be interpreted as a transition to the structure of Cr_5S_6 , caused by a deficiency in S (see Figure S1 and S3, Supporting Information).^[6] But the stoichiometry of the material is still $\approx\text{Cr}_3\text{S}_4$ and reflection positions match with those expected for Cr_2S_3 in $P\bar{3}1c$. Therefore, we conclude from these findings that the defect Cr_3S_4 structure in $R\bar{3}$ space group can transform into the $P\bar{3}1c$ structure when treated at high temperatures for longer time periods and larger x in $\text{Cr}_3\text{S}_{4-x}$.

After sintering, the sample pellets were analyzed concerning their preferred orientation of the crystallites and the data are listed in Table S2 and S5, Supporting Information. The samples show a preferred orientation of the crystallites (002) plane perpendicular to

the uniaxial pressing direction of 7–11%, but this seems to be random and does not correlate with compositions or sinter conditions.

To investigate the microstructure, pieces were cut from the pellets, ground, and analyzed by XRD. After the sintering at different conditions, all Cr_3S_4 samples consist almost purely of Cr_3S_4 in the monoclinic crystal structure (space group $I2/m$; see Figure S5, Supporting Information). Though in samples 1, 2, 6, and 8, formation of the mentioned defect structure of Cr_3S_4 in the $R\bar{3}$ crystal structure is observed with estimated amounts of 3–9 wt%. The formation of the defect phase seems not to correlate with sinter parameters. Additionally, in samples 2, 6, and 7, Cr_2O_3 is observed as an impurity with contents of 1–2 wt%. In summary, the sintering process does not purify the samples as observed for NiCr_2S_4 .^[26]

When comparing samples 1, 3, 6, and 8 (see Table 1 for reference), a dependency of the microstructure and sinter temperature is observable (see Figure 2 and Table S3, Supporting Information). With increasing temperature from 973–1123 K, the unit cell parameter a and monoclinic angle β decrease slightly while the lattice parameters b and c and the unit cell volume remain constant. Other properties like micro-strain or the occupancy of the Cr1 position are not affected.

An increase in sinter pressure from 197 to 395 MPa leads to a slight decrease in the a -axis while other parameters seem to be unaffected (see Figure 3 and Table S3, Supporting Information).

Increasing the duration of the sintering process from 5 to 30 min increases the a -axis and unit cell volume, while the angle β decreases and lattice parameters b and c are not changed (see Figure 4 and Table S3, Supporting Information). Additionally, the occupancy of Cr1 decreases, accompanied by a reduction of the apparent phase density, while micro-strain is also enlarged. Further, the detected amount of the Cr_2S_3 -like defect phase crystallizing in space group $R\bar{3}$ decreases. This observation suggests that the occurrence of the defect phase is a local phenomenon, which can be extended over longer distances via prolonged heat treatment. Note that based on the obtained data, the effects of different sinter pressure, duration, and thermal treatment are interpreted on the basis of two samples each, which only allows for a discussion of trends.

Table 1. Overview of the sintering parameters and physical properties at room temperature of the Cr_3S_4 samples. Relative densities are determined from Rietveld refinements, assuming an ideal density of Cr_3S_4 . Corresponding experimental data for $\text{Cr}_3\text{S}_{4-x}\text{Se}_x$ is presented in Table 2.

Sample	FAST temperature [K]	FAST pressure [MPa]	FAST holding time [min]	Bulk density [g cm^{-3}]	Relative density [%]	Vickers Hardness HV [GPa]	Electrical conductivity [S cm^{-1}]	Seebeck coefficient [$\mu\text{V K}^{-1}$]
1	973	395	5	3.879(19)	94	1.8	910	−30
2	1023	197	5	3.8 ^{a)}	92	2.0	768	−30
3	1023	395	5	3.947(7)	96	1.9	1266	−28
4	1023	395	5	3.950(10)	96	—	1304	−28
5	1073	197	5	3.9 ^{a)}	95	1.6	1194	−28
6	1073	395	5	3.962(4)	96	2.9	973	−30
7	1073	395	30	4.005(5)	97	3.3	1012	−30
8	1123	395	5	4.001(1)	97	2.3	1150	−29

^{a)} Due to the high porosity of the samples, the densities and electrical conductivities could not be measured accurately.

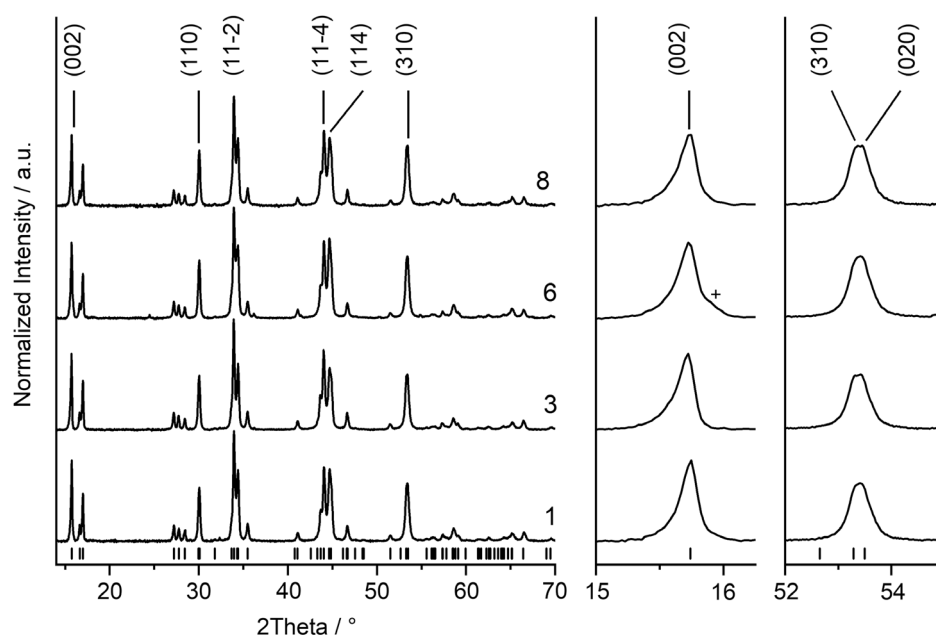


Figure 2. Comparison of normalized X-ray diffraction (XRD) patterns of samples sintered at different temperatures (973, 1023, 1073, and 1123 K bottom to top). Reflection positions of the Cr_3S_4 phase are marked as black bars and visible reflections of the defect phase in space group $\bar{R}3$ as black +. Background is subtracted for clarity.

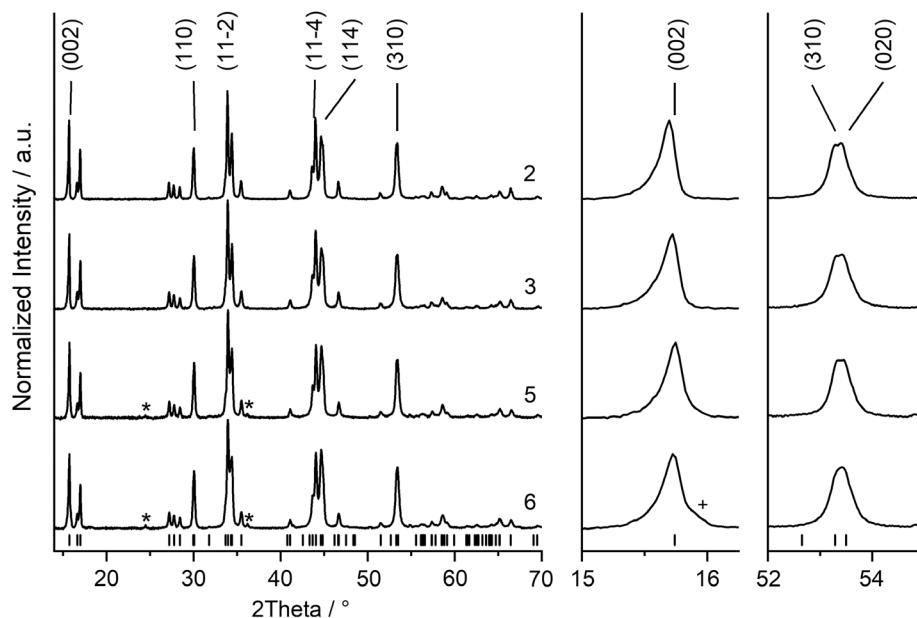


Figure 3. Comparison of normalized XRD patterns of samples sintered at different pressures (3 and 5 at 395 MPa, 2 and 6 at 197 MPa). Reflection positions of the Cr_3S_4 phase are marked as black bars, reflections of the Cr_2O_3 impurity as black *, and visible reflections of the defect phase in space group $\bar{R}3$ as black +. Background is subtracted for clarity.

The substitution of S by Se (sample 4 and 9–13) leads to a linear increase in the unit cell parameters a , b , and c , while the monoclinic angle β is almost constant (see Figure S16 and S20 and Table S6, Supporting Information). Overall, the unit cell volume and phase density increase as expected due to the larger anionic radius and weight of Se^{2-} compared to S^{2-} . However, regarding atomic positions, occupancy of Cr1 or micro-strain

(see Tables S6 and S7, Supporting Information), no clear trend could be observed with increasing Se content. For these samples, no impurity due to a Cr_2S_3 -like defect phase in space group in $\bar{R}3$ is detected, just minor amounts of Cr_2O_3 in samples with low Se content are present. The absence of the defect phase may be related to a larger phase region in the $\text{Cr}_{3\pm 4}\text{Se}_4$ selenides in comparison to Cr_3S_4 ,^[13–16] and that Se substitution leads to a

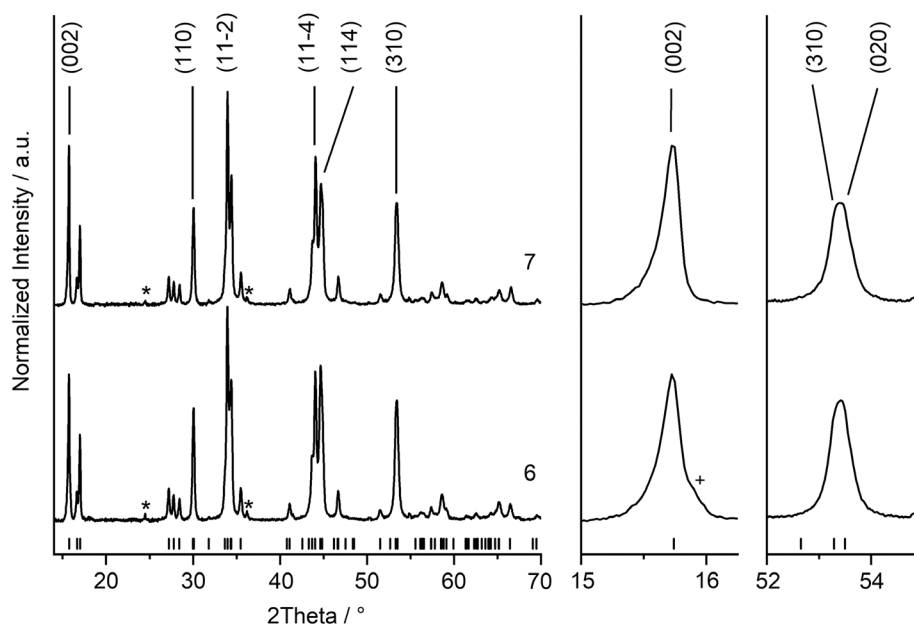


Figure 4. Comparison of normalized XRD patterns of samples sintered for different times (7 for 5 min and 6 for 30 min). Reflection positions of the Cr_3S_4 phase are marked as black bars, reflections of the Cr_2O_3 impurity as black *, and visible reflections of the defect phase in space group $R\bar{3}$ as black +. Background is subtracted for clarity.

broadening of this region in the sulfide. A definitive explanation can, however, not be given at this point.

Temperature-dependent XRD experiments on Cr_3Se_4 in inert atmosphere, though, give evidence for changes during heating, which are irreversible when cooling down (see Figure S21–S23, Supporting Information). Like for Cr_3S_4 , a continuous increase in lattice parameters and unit cell volume occurs when the temperature is increased, while β decreases. Up to 623 K, the expansion of the unit cell correlates linear with temperature (see Figure S22, Supporting Information). The deviation from linear behavior at higher temperatures may be the result of a starting phase transformation and/or a decomposition. Similar to Cr_3S_4 , the occupancy of the Cr1 atomic position irreversibly decreases with temperature, being indicative for a disorder. After cooling, the lattice parameters and unit cell volume are slightly smaller than before the heating process (see Figure S22 and S23, Supporting Information), suggesting that the unit cell contracts during heat treatment of Cr_3Se_4 .

2.2. Transmission Electron Microscopy

To gain insight into the structural inclusion and impact of the Cr_2S_3 -like defect phase, transmission electron microscopy (TEM) investigations have been carried out on sample 1. High-resolution TEM (HRTEM) revealed that the material comprised nanocrystalline grains, varying in sizes between 5 and 20 nm. Via EDX area scans, the overall composition could be determined as 44 at% Cr and 56 at% S, almost perfectly matching the theoretical target composition of 43:57 at% Cr to sulfur, respectively. Due to this, it can be assumed that no larger-scale areas with a significant Cr deficiency are present in the sample,

which may be a cause for the defect phase. Another possibility is that the defect phase occurs highly localized within a few nanometer rather than on a larger scale, which was subsequently investigated via probe-corrected scanning TEM (STEM). As shown in Figure 5a (arrow), nanoscale areas with darker Z-contrast could be identified in the material, containing an overall lighter atomic weight and therefore, presumably, a deficiency in Cr. This could be verified through an EDX area scan (Figure 5a, rectangle), with the results being shown in Figure 5b: while the surrounding material matched the targeted composition for Cr_3S_4 , the area with a darker Z-contrast exhibited a notably different composition (see distance of 65–75 nm in Figure 5b). The determined composition of ≈ 40 at% Cr to 60 at% S matches that of Cr_2S_3 , which leads to the assumption that the defect phase occurs on a similar length scale as singular grains.

Selected area electron diffraction (SAED) was used to determine the crystal structure of the sample as well as that of the defect phase. In large-scale diffraction patterns, as shown in Figure 6a, the main material could be identified as Cr_3S_4 in its monoclinic equilibrium phase (space group: $I2/m$). However, two further reflections could be identified and attributed to trigonal Cr_2S_3 crystallizing in space group $R\bar{3}$. Both reflections are visible in the diffraction pattern's intensity profile shown in Figure 6b, and could be indexed as the $(0\bar{1}1)$ and $(\bar{1}02)$ reflections, respectively. In further diffraction experiments, a grain of the defect phase could be imaged, with the corresponding pattern being shown in Figure 6c. The pattern could be matched to zone axis $[1\bar{1}1]$ of Cr_2S_3 in the $R\bar{3}$ phase, with the d -values generally appearing slightly smaller than in literature.^[4] In several directions, that is, $(033)^*$, $(\bar{3}36)^*$, and $(\bar{3}03)^*$, the

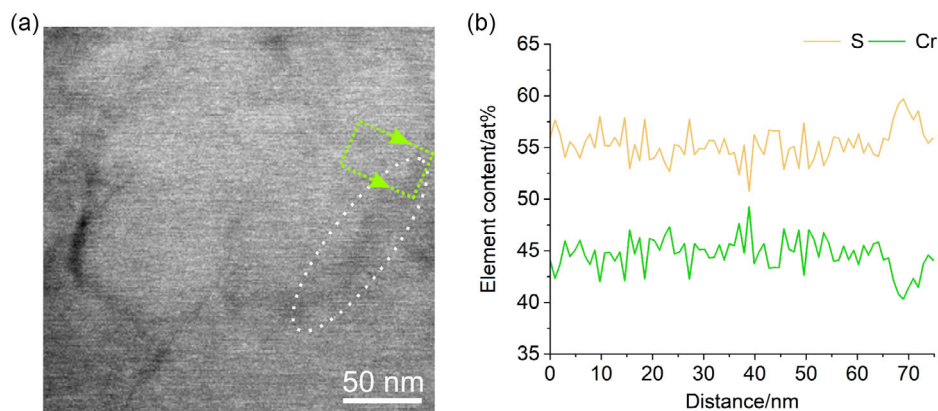


Figure 5. a) Scanning transmission electron microscopy (STEM) micrograph of sample 1. An area exhibiting a dark Z-contrast could be detected (white ellipsis), which corresponds to a lower atomic weight than the surrounding material. An energy-dispersive X-ray spectroscopy (EDX) elemental mapping was obtained from the rectangular region marked in green. b) EDX scan profile extracted from the mapping marked in (a), measured and drawn from left to right (arrows). Most of the material corresponds to the targeted composition of Cr_3S_4 with ≈ 44 at% Cr and 56 at% S, respectively. The area with darker Z-contrast (65–75 nm distance) exhibits a composition of ≈ 40 at% Cr and 60 at% S, matching the composition of Cr_2S_3 .

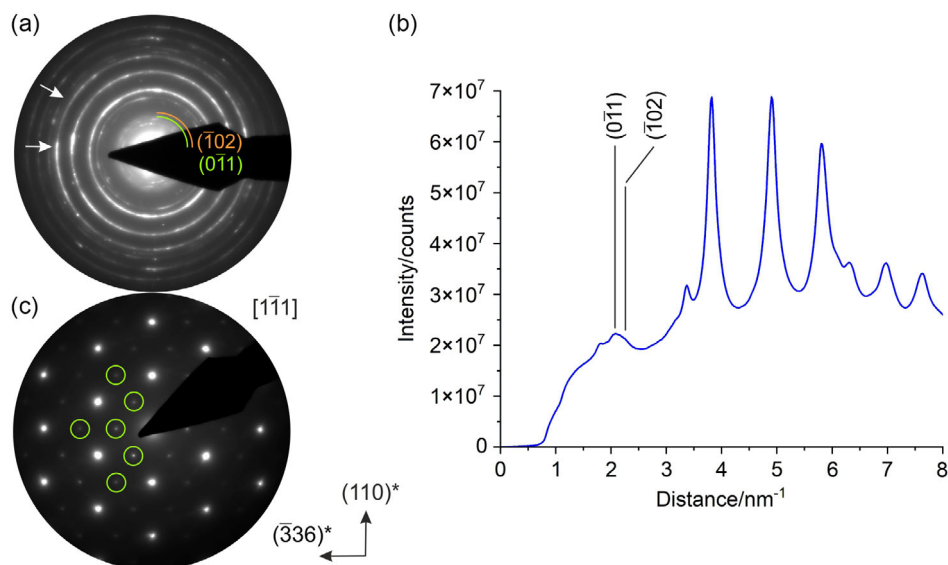


Figure 6. a) Electron diffraction pattern of sample 1 (polycrystalline), mainly corresponding to Cr_3S_4 in its equilibrium phase. White arrows exemplify variations in reflection intensity corresponding to texturing. Additional reflections of the Cr_2S_3 -like defect phase could be detected and are indicated at the respective reflection positions (green and orange). b) Intensity profile of the diffraction pattern in (a) with distance measured from the pattern center outward. Reflections matching to Cr_2S_3 are indicated, with the $(\bar{1}02)$ reflection being visible as a shoulder of the $(0\bar{1}1)$ reflection. c) Electron diffraction pattern (single crystalline) of a grain in the Cr_2S_3 -like defect phase. Main reflections correspond to the equilibrium phase ($R\bar{3}$) in zone axis $[1\bar{1}1]$, with additional reflections appearing along several directions (green circles), indicating a tripling of the lattice parameters.

appearance of additional reflections could be observed (Figure 6c, green circles), causing a tripling of the lattice parameter. The tripled parameter does not correspond to the $R\bar{3}$ equilibrium phase, but occurs in the second polytype of Cr_2S_3 with space group $P\bar{3}1c$. This polytype has been observed to occur after an electron beam-induced phase transformation of Cr_2S_3 , which has been reported in previous studies.^[25,30]

A general TEM investigation has also been performed on a sample with the nominal composition $\text{Cr}_3\text{S}_2\text{Se}_2$, to determine the general composition and structure after substitution. No

significant deviations in stoichiometry could be identified via EDX, with d -values determined via SAED generally being measured right between those of Cr_3S_4 and Cr_3Se_4 .

2.3. Thermoelectric Properties at RT for Cr_3S_4

As expected, a higher sintering temperature or applied pressure results in denser samples (Table 1). A comparison of the samples 2 and 3 shows that at the same sintering temperature, increasing the applied pressure can significantly improve the densification

and thus the thermoelectric properties. For good compaction of the powders, a temperature of at least 1023 K and an applied pressure of 395 MPa is required. The electrical conductivities vary greatly among the samples between 768 and 1266 S cm⁻¹. The Seebeck coefficient also varies, but as expected for a metal, the values are at a very low level between -28 and -30 μV K⁻¹. Due to the poorer compaction, the samples 1 and 2 have the lowest electrical conductivity. Overall, however, there is no correlation between the thermoelectric properties and the sintering parameters. Rather, the partially present defect phase has a strong influence on the electrical conductivity (Figure 7). The higher the proportion of this defect phase, the lower the electrical conductivity and the higher the Seebeck coefficient. This becomes particularly clear when comparing samples 5 and 6. Despite the higher density of sample 6, it has a lower electrical conductivity than sample 5 due to the higher proportion of the defect phase.

To investigate the influence of substitution of S with Se, the powders were sintered under the same conditions, that is, Cr₃S_{3-x}Se_x was sintered via FAST at 1023 K and 395 MPa for 5 min. Due to the higher molar mass of Se compared to S, the bulk density increases with higher amount of Se (Table 2). The relative density is between 94% and 97%, indicating good sintering characteristics. Generally, the substitution with Se leads to a decrease in electrical conductivity, whereas the Seebeck coefficient remains largely unaffected. Only sample 9 with the lowest proportion of Se shows a slight increase in α . Furthermore, this sample has the lowest electrical conductivity at RT with 480 S cm⁻¹, which overall indicates a reduction of the charge carrier concentration.

2.4. Thermal Treatment and Electric Properties

2.4.1. Cr₃S₄

The electrical conductivity of sample 7 generally deteriorated with each measurement and especially after annealing, while the Seebeck coefficient remained stable (Figure 8). Before sintering, a defect phase could already be identified in the sample. With each temperature treatment, the proportion of this phase increases and the conductivity is further reduced. As a result, the electrical conductivity decreases by 10% after the first annealing compared to the value before the temperature treatment. After the second annealing, a reduction of only 4% is observed.

For comparison, the long-term stability of the phase-pure sample 4 was investigated, and the thermoelectric properties of this sample were measured three times (Figure 9). As expected for a metallic conductor, the electrical conductivity decreases from around 1300 S cm⁻¹ at RT to 960 S cm⁻¹ at 773 K. In contrast, the Seebeck coefficient slightly increases up to -51 μV K⁻¹ at 773 K. Unusually, the thermal conductivities increase with temperature from 2.3 at RT to 3–3.3 W m⁻¹ K⁻¹ at 723 K. A similar behavior has already been observed for Cr₂S₃.^[30] Overall, the values for the thermoelectric figure of merit (ZT) are at a very low level with 0.01 at RT and a maximum of 0.06 at 723 K. Although in the non-sintered sample the defect phase could be identified at 623 K by in situ XRD, no differences in the values between the measurements can be observed. Thus, the sintering appears to have a positive effect on the structural stability and prevents

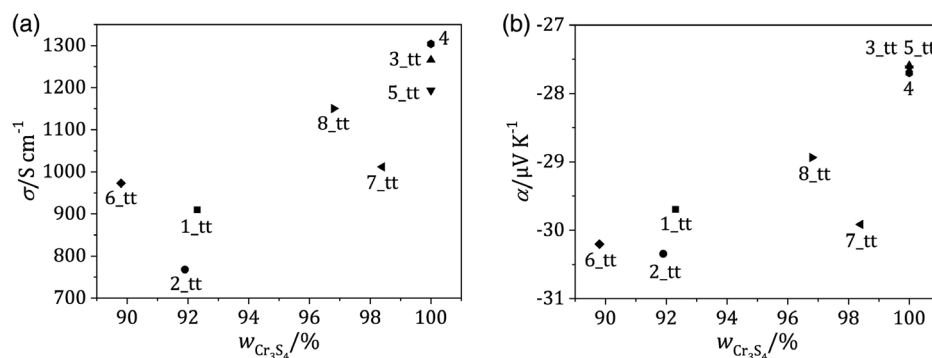


Figure 7. Correlation of the mass fraction w of Cr₃S₄ to a) the electrical conductivity σ and b) the Seebeck coefficient α . With the exception of sample 6, all samples were annealed twice. These samples are labeled as “tt”.

Table 2. Overview of the physical properties at room temperature of the substituted Cr₃S₄ samples. Relative densities are determined from Rietveld refinements, assuming an ideal density.

Sample	Chemical composition	Symbol	Bulk density [g cm ⁻³]	Relative density [%]	Electrical conductivity [S cm ⁻¹]	Seebeck coefficient [μV K ⁻¹]
4	Cr ₃ S ₄	Cr ₃ S ₄	3.950(10)	96.0	1304	-28
9	Cr ₃ S _{3.5} Se _{0.5}	Se05	4.133(18)	94.1	480	-37
10	Cr ₃ S ₃ Se ₁	Se10	4.385(11)	95.5	683	-28
11	Cr ₃ S _{2.5} Se _{1.5}	Se15	4.638(13)	96.5	760	-28
12	Cr ₃ S ₂ Se ₂	Se20	4.854(14)	96.4	765	-29
13	Cr ₃ Se ₄	Cr ₃ Se ₄	5.718(4)	97.3	1079	-30

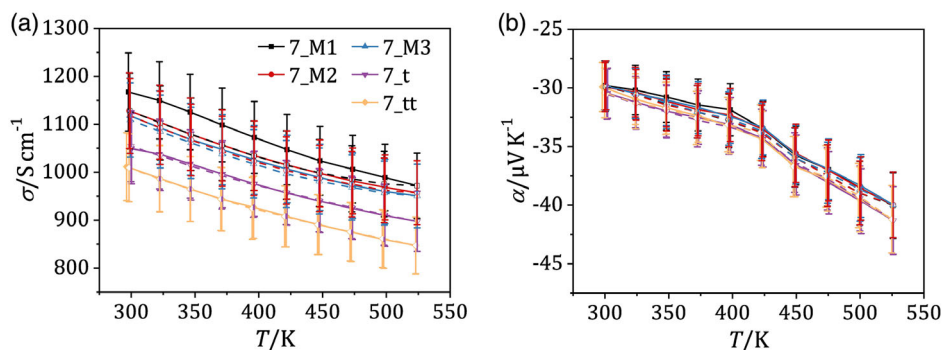


Figure 8. a) Influence of annealing on electrical conductivity and b) Seebeck coefficient of sample 7, sintered at 1073 K and 395 MPa for 30 min. The sample was measured three times before annealing (M1–M3) and once each after the first (7_t) and second annealing (7_tt).

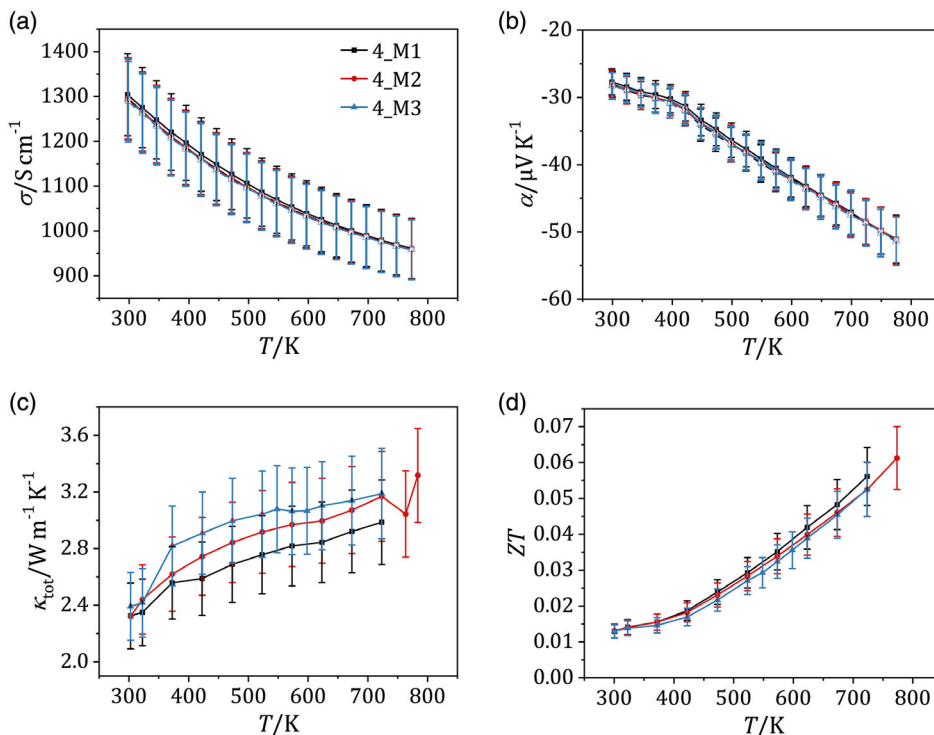


Figure 9. Influence of thermal cycling on the thermoelectric properties of sample 4, divided into a) electrical conductivity σ , b) Seebeck coefficient α , c) total thermal conductivity κ_{tot} , and d) ZT . M1–M3 indicate subsequent thermal cycles, while solid lines indicate heating and dashed lines cooling procedures, respectively.

the formation of the defect phase if it was not yet present at RT. It can further be assumed that a small over-stoichiometric surplus in S is also beneficial for phase purity, as it negates the volatilization loss during treatment.

2.4.2. $\text{Cr}_3\text{S}_{4-x}\text{Se}_x$

Substitution with Se had a noticeable influence on the thermoelectric properties, with values at RT being shown in Table 2. **Figure 10** displays the results of the thermoelectric measurements up to a temperature of 773 K. For all samples, the electrical conductivity decreases with temperature, indicating metallic conduction. It is noticeable that the electrical

conductivity does not decrease as much as expected. In the measured temperature range, σ usually follows a T^{-1} curve due to the electron–phonon scattering. The substitution with Se leads to a reduction of σ to as low as 480 S cm^{-1} at RT. With increasing amount of Se, the electrical conductivity increases up to 1079 S cm^{-1} at RT in Cr_3Se_4 . The Seebeck coefficient increases slightly with the temperature. All samples have a very similar Seebeck coefficient, which is around $-50 \mu\text{V K}^{-1}$ at 773 K. The exception is sample 9, which has a slightly larger Seebeck coefficient and reaches the best value of all samples with $-67 \mu\text{V K}^{-1}$ at 773 K. The substitution with Se lowers the thermal conductivity to as low as $1.6 \text{ W m}^{-1} \text{K}^{-1}$ compared to pure Cr_3S_4 with $2.3 \text{ W m}^{-1} \text{K}^{-1}$.

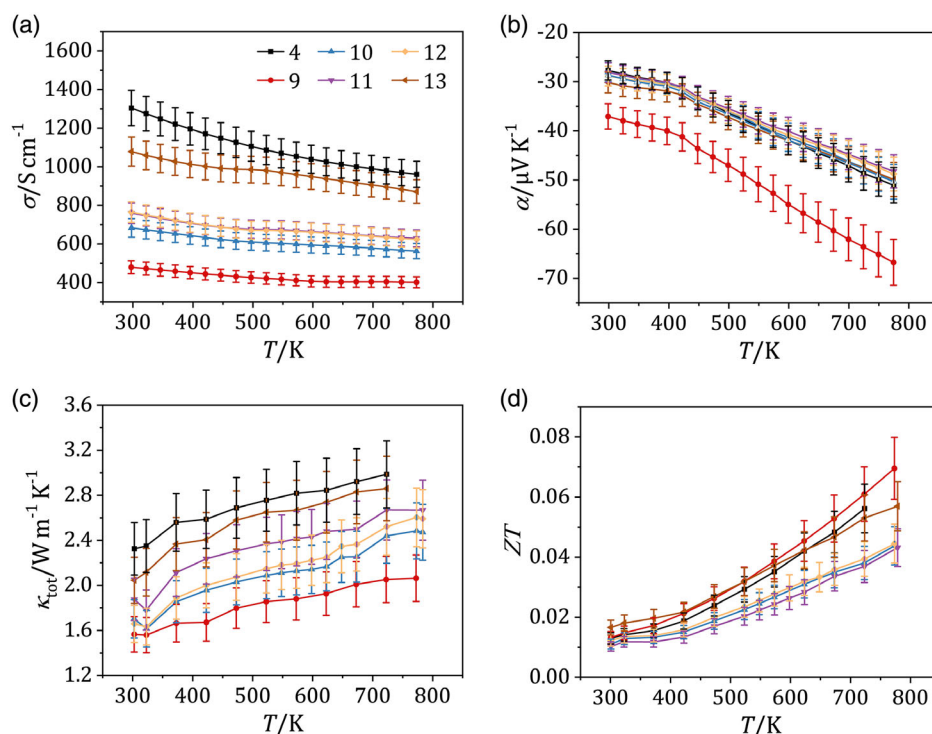


Figure 10. Temperature dependence of the a) electrical conductivity σ , b) Seebeck coefficient α , c) thermal conductivity κ_{tot} , and d) ZT for the $\text{Cr}_3\text{S}_{4-x}\text{Se}_x$ samples.

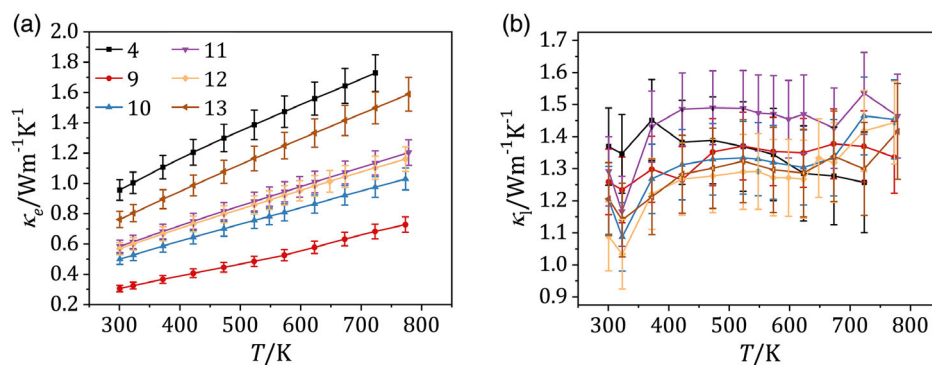


Figure 11. a) Electronic κ_e and b) lattice thermal conductivity κ_l of the $\text{Cr}_3\text{S}_{4-x}\text{Se}_x$ samples.

The values for ZT are on a similar low level with values between 0.01 and 0.02 at RT. The ZT values increase with temperature, with sample 9 reaching the highest value at 773 K with 0.07. As already observed for Cr_3S_4 , the thermal conductivities increase with the temperature.

For a more detailed investigation, the electronic and lattice thermal conductivities were calculated according the Wiedemann–Franz law ($\kappa_e = L\sigma T$) using the constant Lorenz number for metals of $L = 2.44 \times 10^{-8} \text{ V}^2 \text{ K}^{-2}$ (see Figure 11). Since the electrical conductivity does not follow the T^{-1} curve expected due to electron–phonon scattering, the electronic part and thus the thermal conductivity increase with temperature. Furthermore, the lattice thermal conductivity remains almost independent of the temperature and does not decrease due to the expected Umklapp scattering. One reason could be the partially occupied metal layers and

the associated defect-rich structure. The substitution with Se and the resulting solid solutions have no influence on the lattice thermal conductivity. Rather, the reduction of the total thermal conductivity is due to the decrease in electrical conductivity and thus the electronic thermal conductivity.

3. Conclusion

The occurrence of a Cr_2S_3 -like defect phase in Cr_3S_4 could be proven to significantly impact both microstructure and electrical properties. If traces of the defect phase were present before sintering, they could not be removed in the process and only be reduced with prolonged sintering durations. TEM studies showed that the defect phase is highly localized with domains

in a size range of 5–10 nm. These were found in most of the material and can be assumed to occur as a fine dispersion. The defect phase itself appeared as unstable and could undergo a phase transformation from its equilibrium space group $R\bar{3}$ to $P\bar{3}1c$. The material with the defect phase shows a decrease in electrical conductivity, with a slight improvement of the Seebeck coefficient. Annealing and heat treatment led to a further decrease in electrical conductivity, as the fraction of the defect phase increase. Phase-pure material could be stabilized via sintering and showed stable electrical properties during cycling and heat treatment. Substituting S with Se led to a suppression of the defect phase and a reduction in both electrical and thermal conductivity, the latter being improved mainly by a reduction in the electrical contribution to thermal conductivity. Lower levels of substitution generally exhibited the highest impact on the electrical properties, however, no substantial overall improvements in ZT could be made.

4. Experimental Section

Synthesis: As starting materials, chromium powder (Alfa Aesar, 60 mesh, 99.99%), selenium granules (Chempur, >99.99%), sulfur pieces (Alfa Aesar, 99.9995%), and NH_4Br were used as obtained.

The Cr_3S_4 was synthesized in several batches by thoroughly mixing the elements in stoichiometric ratios and placing the powder in evacuated quartz ampoules. These ampoules were heat-treated in a muffle furnace by heating them to 723 K in 960 min, dwelling them for 1 d, followed by heating to 1273 K in 2 d and dwelling for 3 d. Finally, the ampoules were cooled down to RT, cut open and the enclosed melt body was ground and analyzed with XRD for testing on phase purity.

Samples of the series $\text{Cr}_3\text{S}_{4-x}\text{Se}_x$ were synthesized in three batches per composition by mixing stoichiometric amounts of Cr, S, and Se, adding a little excess of chalcogenides and placing the powder in evacuated quartz ampoules. The ampoules were heated up to 723 K within 960 min in a muffle furnace and dwelled at that temperature for 1 d. The temperature was then increased to 953 K within 720 min and again the temperature was held for 1 d. Finally, the temperature was raised to 1273 K within 720 min and kept for 3 d before uncontrolled cooling down to RT. The samples were ground and mixed with 10 mg NH_4Br and again placed in evacuated quartz ampoules and heated up to 1273 K in 1 d and dwelled at that temperature for 3 d. After uncontrolled cooling, the samples were ground in Ar atmosphere.

The phase-pure Cr_3S_4 powder was sintered using a FAST equipment “HP D 5” by FCT Systems GmbH. To realize the sintering at several hundred MPa, the main components of the FAST apparatus, including die, punches, and spacers, were made of a TZM alloy by Wagener GmbH. To determine the optimal sintering parameters, both temperature (973–1123 K) and the applied pressure were varied (197 or 395 MPa). To avoid possible evaporation of sulfur, a high heating and cooling rate of 100 K min^{-1} and a short holding time of 5 min were applied. The resulting samples had a diameter of 12.7 mm. After sintering, some samples were annealed in two runs. In the first run, the samples were heated for 24 h, in the second for 48 h. In both cases, the annealing was done at 523 K under argon atmosphere.

X-Ray Diffraction and Rietveld Refinements: For XRD analysis in the as-synthesized state, a PAN'alytical Empyrean MPD was employed, using $\text{Cu K}\alpha$ irradiation.

After sintering the materials via FAST, the obtained pellets were analyzed for preferred orientation with a PAN'alytical X'Pert MPD, using $\text{Cu K}\alpha$ irradiation in Bragg–Brentano geometry. The X-ray beam was altered using a $1/4^\circ$ divergence slit, a 10 mm mask, 0.04 rad Soller slit, a Goebel mirror, and a $1/2^\circ$ anti-scatter slit. Scattered X-ray beams were treated with a parallel plate collimator and a Ni filter.

For a more detailed Rietveld analysis, parts of the pellets were ground, mixed with amorphous SiO_2 , and filled in glass capillaries of 0.2 mm in diameter and the XRD pattern was collected with a PAN'alytical

Empyrean MPD using $\text{Cu K}\alpha$ irradiation. The X-ray beam was altered with a $1/4^\circ$ divergence slit, a 20 mm mask, a 0.04 rad Soller slit, a focusing mirror and a $1/2^\circ$ anti-scatter slit. Scattered X-ray beams were treated with a 0.04 rad Soller slit and Ni Filter.

Rietveld refinements were done using the program TOPAS v6^[31] in combination with coding program jedit v4.3.^[32] The reflection profiles were modeled with the implemented fundamental parameter approach of TOPAS. Structural data was obtained from crystallographic data of Cr_2S_3 (ICSD 16721^[4]), Cr_3S_4 (ICSD 16722^[17]), and graphite (ICSD 31170^[33]).

Preferred orientation was considered using the TOPAS-implemented macro “Preferred Orientation 1D” in (00L) direction. The obtained r value was transformed into a percentual value with the method of March–Dollase^[34,35] supplemented by Zolotoyabko.^[36]

Transmission Electron Microscopy: TEM studies were performed on an FEI Tecnai F30 G² with a field-emission gun (FEG) at 300 kV and $C_s = 1.2\text{ mm}$, which included an EDAX Si/Li detector for EDX. Additional EDX investigations were carried out on a JEOL JEM-ARM200F NEOARM operated with a cold FEG at 200 kV and dual silicon drift detectors with each 100 mm^2 for EDX analysis. Sample 1 was prepared for analysis via conventional preparation using bulk material taken from the sample pellet. The material was subsequently thinned by mechanical grinding and dimpling, followed by polishing with Ar ions in a Gatan Precision Ion Polishing System (PIPS). Other samples were prepared as powders and drop-coated on Al grids using butanol as suspending medium. Experimental TEM data was evaluated using Gatan Digital Micrograph with additional scripts described in Ref. [37].

Density and Electronic Properties: An Archimedes setup with ethanol was used to determine the bulk densities at RT. The resulting values were averaged from four measurements of each sample. The uncertainty was calculated via the standard deviation. The relative densities were calculated as a ratio of the measured density to the density calculated via Rietveld refinements $\rho_{\text{obs}}/\rho_{\text{XRD}}$, considering calculated unit cell volume and Cr_3S_4 stoichiometry. The electrical conductivity and the Seebeck coefficient were measured perpendicular to the pressing direction using the Netzsch SBA 458 Nemesis under Ar or N_2 atmosphere with an uncertainty of 7%. The thermal conductivity κ was determined according to $\kappa(T) = \rho(T) \times c_p(T) \times a(T)$, with the density ρ , the specific heat c_p , and the thermal diffusivity a with an uncertainty of 10%. The thermal diffusivity was measured parallel with the Netzsch LFA 457 MicroFlash under Ar atmosphere and the specific heat was determined by using a reference specimen (Figure S24, Supporting Information). Due to the random orientation of the crystallites, the direction of measurement has no significant influence on the calculation of the ZT value.

Supporting Information

Supporting Information is available from the Wiley Online Library or from the author.

Acknowledgements

H.G. and D.G. contributed equally to this work. The authors gratefully acknowledge funding by the German Research Foundation (DFG) within the research grants BE 1653/36-1, KI 1263/16-1, and KO 5397/2-1.

Open Access funding enabled and organized by Projekt DEAL.

Conflict of Interest

The authors declare no conflict of interest.

Data Availability Statement

The data that support the findings of this study are available from the corresponding author upon reasonable request.

Keywords

anion substitution, chromium chalcogenides, phase relations, thermoelectricity

Received: October 17, 2022

Revised: December 8, 2022

Published online: February 15, 2023

- [1] A. Maignan, E. Guilmeau, F. Gascoin, Y. Bréard, V. Hardy, *Sci. Technol. Adv. Mater.* **2012**, 13, 053003.
- [2] A. Maignan, Y. Bréard, E. Guilmeau, F. Gascoin, *J. Appl. Phys.* **2012**, 112, 013716.
- [3] Z.-H. Ge, L.-D. Zhao, D. Wu, X. Liu, B.-P. Zhang, J.-F. Li, J. He, *Mater. Today* **2016**, 19, 227.
- [4] F. Jellinek, *Acta Crystallogr.* **1957**, 10, 620.
- [5] P. Vaquero, A. V. Powell, *Chem. Mater.* **2000**, 12, 2705.
- [6] S. L. Holt, R. J. Bouchard, A. Wold, *J. Phys. Chem. Solids* **1966**, 27, 755.
- [7] Y. Tazuke, *Phys. Lett. A* **1979**, 69, 341.
- [8] Y. Noda, *J. Common Met.* **1981**, 80, 165.
- [9] P. Waldner, W. Sitte, *Int. J. Mater. Res.* **2011**, 102, 1216.
- [10] D. J. Young, W. W. Smeltzer, J. S. Kirkaldy, *J. Electrochem. Soc.* **1973**, 120, 1221.
- [11] H. Rau, *J. Common Met.* **1977**, 55, 205.
- [12] C. F. van Bruggen, Ph.D. thesis, Rijksuniversiteit Groningen **1969**.
- [13] T. Ohtani, R. Fujimoto, H. Yoshinaga, M. Nakahira, Y. Ueda, *J. Solid State Chem.* **1983**, 48, 161.
- [14] M. Wintenberger, G. André, J. Hammann, *J. Magn. Magn. Mater.* **1995**, 147, 167.
- [15] A. Maurer, G. Collin, *J. Solid State Chem.* **1980**, 34, 23.
- [16] F. H. Wehmeier, E. T. Keve, S. C. Abrahams, *Inorg. Chem.* **1970**, 9, 2125.
- [17] D. C. Colgan, A. V. Powell, *J. Mater. Chem.* **1996**, 6, 1579.
- [18] R. J. Bouchard, A. Wold, *J. Phys. Chem. Solids* **1966**, 27, 591.
- [19] A. V. Powell, P. Vaquero, A. McDowall, *Solid State Ion.* **2004**, 172, 469.
- [20] D. P. Spitzer, *J. Phys. Chem. Solids* **1970**, 31, 19.
- [21] D. M. Rowe, in *CRC Handbook of Thermoelectrics*, CRC Press, Boca Raton, FL **2018**.
- [22] G. J. Snyder, T. Caillat, J.-P. Fleurial, *MRS Online Proc. Libr. OPL* **1998**, 545, 333.
- [23] V. A. Ivanova, D. Sh. Abdinov, G. M. Aliev, *Phys. Status Solidi B* **1967**, 24, K145.
- [24] J. Koenig, M. Winkler, T. Dankwort, A.-L. Hansen, H.-F. Pernau, V. Duppel, M. Jaegle, K. Bartholomé, L. Kienle, W. Bensch, *Dalton Trans.* **2015**, 44, 2835.
- [25] D. Groeneveld, H. Groß, A.-L. Hansen, T. Dankwort, J. Hansen, J. Wöllenstein, W. Bensch, L. Kienle, J. König, *Adv. Eng. Mater.* **2019**, 21, 1900430.
- [26] H. Groß, T. Dankwort, A.-L. Hansen, U. Schürmann, V. Duppel, M. Poschmann, A. Meingast, D. Groeneveld, J. König, W. Bensch, L. Kienle, *J. Mater. Chem. C* **2019**, 7, 15188.
- [27] H. Groß, M. Poschmann, D. Groeneveld, J. D. Koenig, L. Kienle, W. Bensch, *Adv. Eng. Mater.* **2022**, 24, 2100828.
- [28] K. R. Pisharody, *J. Solid State Chem.* **1979**, 30, 149.
- [29] D. Babot, M. Chevreton, *J. Solid State Chem.* **1973**, 8, 166.
- [30] H. Groß, Y. Ekici, M. Poschmann, D. Groeneveld, T. Dankwort, J. D. Koenig, W. Bensch, L. Kienle, *J. Electron. Mater.* **2022**, 51, 3510.
- [31] A. Coelho, Topas Academic V6, Coelho Software, **2016**.
- [32] jEdit - Programmer's Text Editor - Overview, <http://www.jedit.org/> (accessed: February 2023).
- [33] O. Hassel, H. Mark, *Z. Für Phys.* **1924**, 25, 317.
- [34] A. March, *Z. Für Krist. – Cryst. Mater.* **1932**, 81, 285.
- [35] W. A. Dollase, *J. Appl. Crystallogr.* **1986**, 19, 267.
- [36] E. Zolotoyabko, *J. Appl. Crystallogr.* **2009**, 42, 513.
- [37] D. R. G. Mitchell, B. Schaffer, *Ultramicroscopy* **2005**, 103, 319.
- [38] K. Momma, F. Izumi, *J. Appl. Crystallogr.* **2008**, 41, 653.